

First-principles determination of the phonon-point defect scattering and thermal transport due to fission products in ThO₂

Linu Malakkal^{1,*}, Ankita Katre^{2,†}, Shuxiang Zhou¹, Chao Jiang¹, David H. Hurley³,
Chris A. Marianetti⁴, and Marat Khafizov^{5,‡}

¹Computational Mechanics and Materials Department, Idaho National Laboratory, Idaho Falls, Idaho 83415, USA

²Department of Scientific Computing, Modeling and Simulation, SP Pune University, Pune 411007, India

³Idaho National Laboratory, Idaho Falls, Idaho 83415, USA

⁴Department of Applied Physics and Applied Mathematics, Columbia University, 500 West 120th Street, New York, New York 10027, USA

⁵Department of Mechanical and Aerospace Engineering, The Ohio State University, 201 West 19th Avenue, Columbus, Ohio 43210, USA



(Received 30 August 2023; accepted 18 January 2024; published 8 February 2024)

This work presents the first-principles calculations of the lattice thermal conductivity degradation due to point defects in thorium dioxide using an iterative solution of the Peierls-Boltzmann transport equation. We have used the nonperturbative Green's function methodology to compute the phonon-point defect scattering rates that consider the local distortion around the point defect, including the mass difference changes, interatomic force constants, and structural relaxation near the point defects. The point defects considered in this work include the vacancy of thorium (V_{Th}) and oxygen (V_{O}), substitutions of helium (He_{Th}), krypton (Kr_{Th}), zirconium (Zr_{Th}), iodine (I_{Th}), and xenon (Xe_{Th}) in the thorium site, and the three different configurations of the Schottky defects. The results of the phonon-defect scattering rate reveal that among all the considered intrinsic defects, the thorium vacancy and helium substitution in the thorium site scatter the phonon most due to the substantial changes in the force constant and structural distortions. The scattering of phonons due to the substitutional defects unveils that the zirconium atom scatters phonons the least, followed by xenon, iodine, krypton, and helium. This is contrary to the intuition that the scattering strength follows $\text{He}_{\text{Th}} > \text{Kr}_{\text{Th}} > \text{Zr}_{\text{Th}} > \text{I}_{\text{Th}} > \text{Xe}_{\text{Th}}$ based on the mass difference. This striking difference in the zirconium phonon scattering is due to the local chemical environment changes. Zirconium is an electropositive element with valency similar to thorium and, therefore, can bond with the oxygen atoms, thus creating less force constant variance compared to iodine, an electronegative element, and the noble gases helium, xenon, and krypton. These results can serve as a benchmark for analytical models and help the engineering-scale modeling effort for nuclear design.

DOI: [10.1103/PhysRevMaterials.8.025401](https://doi.org/10.1103/PhysRevMaterials.8.025401)

I. INTRODUCTION

Thorium dioxide (ThO₂) is expected to play a vital role as a material for advanced nuclear fuel cycles in future energy needs and is considered a better and safer alternative to the currently used uranium dioxide [1]. Since the thermal conductivity of nuclear fuel determines the efficiency and safety of a nuclear reactor, it is imperative to understand the thermal transport of ThO₂ in all possible reactor conditions [2]. It is well known that point defects are ubiquitous in irradiated materials and can scatter phonons, causing a significant reduction in the material's thermal conductivity, especially at low temperatures or high defect concentrations [3]. Enormous efforts are being undertaken to accurately model and ultimately control the thermal transport in nuclear fuels. A detailed description of the new computational and experimental tools for the same is detailed in a recent review article [2]. However, a fundamental understanding of how different fission products

scatter the phonons in nuclear fuels is still lacking. Therefore, an accurate prediction of the phonon-point defect scattering rate by first-principles calculations is imperative to shed light not only on the fundamental physics of phonon transport in irradiated fuels, but also in modeling the thermal transport of ThO₂ during regular operation and accident conditions in a nuclear reactor.

The scattering of phonons by point defects is described as a perturbation to harmonic lattice dynamics. The responsible mechanisms include the mass difference, harmonic force constant changes, and strain field surrounding the defect, often captured by ionic radius difference [4,5]. So far, the widely used description of the phonon-point defect scattering is based on the seminal work by Klemens [6]. In this model, Klemens derived the analytical expression for the phonon elastic scattering cross section by point defects, dislocations, and the grain boundary using second-order perturbation theory. However, the Klemens model is restricted to small perturbations due to mass variance, and the equations are derived assuming a single atom unit cell and linear phonon dispersion [7–10]. Another popular mass difference model used to describe phonon scattering by point defects utilizing realistic phonon dispersion was implemented by Tamura [11]. The

*linu.malakkal@inl.gov

†ankitamkatre@gmail.com

‡khafizov.1@osu.edu

main difference between the Klemens and Tamura models is that the mass difference term in the Tamura model is weighted by the eigenvector components corresponding to the atom in the incident and final vibrational modes. The Born approximation is another standard method that treats the defect using lowest-order perturbation theory [12]. These models become questionable for point defects with large force constant variance and structural changes [13] (i.e., for conditions beyond the low-order perturbation regime). Hence, defining the phonon-defect scattering by a nonperturbative method that includes the scattering due to large variance in force constants becomes vital. Recently, an exact calculation of the phonon-defect scattering rate using the Green's function approach, which is nonperturbative and includes the interatomic force constants (IFCs), has been proposed [14,15]. To date, this method has been successfully used to describe the phonon scattering by point defects in various materials, such as diamond [16], boron arsenide [17], silicon carbide [18], gallium nitride [19], graphene [20], and indium nitride [13]. These calculations have already identified shortcomings of the simplified perturbative methods. They have been instrumental in providing fundamental insights into the phonon-defect scattering of the respective materials.

In ThO_2 , where there is a colossal mass difference between the constituent atoms and the possibility of sizable interatomic force constant differences with point defects, it becomes essential to describe the phonon scattering by point defects with the Green's function methodology. To our knowledge, Green's-function-based methods are not usually employed to study thermal transport in any actinide materials. In the literature, a few first-principles investigations of the thermal conductivity by iteratively solving the Pierels-Boltzmann transport equation of the defect-free ThO_2 are available [21–24]. In 2018, Liu *et al.* [21], using the generalized gradient approximation (GGA) pseudopotential, computed the second-order force constant from the finite-difference method and predicted the thermal conductivity of ThO_2 at 300 K to be 12.4 W/mK, which was underpredicted by $\approx 40\%$ in comparison with experimental results (20.4 W/mK at 300 K) for a single crystal [25]. The following year, using the GGA pseudopotential, Malakkal *et al.* [22] reported a thermal conductivity of 15.4 W/mK at 300 K (underpredicted by $\approx 25\%$) by computing the second-order force constant using the density functional perturbation theory. Using the local density approximation (LDA) pseudopotential, Jin *et al.* [23] predicted a thermal conductivity of 18.6 W/mK (underpredicted by $\approx 9\%$) at room temperature. Recently, Xiao *et al.* [24] calculated the phonon lifetimes and thermal conductivity of ThO_2 with the strongly constrained and approximately normed functional [26] with excellent agreement to experiments, indicating that, over the years, researchers were able to provide a good description of the thermal transport in the pristine ThO_2 using the first-principles simulations by refining the accuracy of calculated interatomic forces.

In practical application such as nuclear fuel, a variety of lattice defects are formed, including the point defects, small defect clusters, and other extended defects such as dislocation loops, inert gas bubbles, grain subdivision induced grain boundaries, and defect segregation at grain boundaries, which

all scatter the phonons and hinder the thermal transport [2]. Until recently, the impact of many of these defects on thermal transport has been treated empirically. To predict temperature distribution within the fuel elements, it is imperative to have a fundamental understanding of the role played by each of these defect types on thermal conductivity [27]. However, to isolate the impact of different defects on thermal transport, it is more practical to consider the low-temperature thermal conductivity. At high temperature, intrinsic three-phonon scattering dominates the reduction of thermal conductivity. At low cryogenic temperatures, the three-phonon scattering is weaker and defect scattering becomes dominant. As a step towards systematically understanding the influence of various defects on the thermal transport, we begin by focusing on the role played by the irradiation-induced small-scale point defects because, at the early stages of damage accumulation, these small-scale lattice defects significantly impact the thermal conductivity [28,29]. Although the main irradiation-induced point defects in nuclear fuels include vacancies, interstitials, fission product acting as substitutions, Frenkel pairs, and the Schottky defects, this work focuses on the impact of vacancies, substitution of fission products, and three different configurations of the Schottky defects. The role of interstitials and Frenkel pairs requires additional code development and will be the subject of future work.

Multiple researchers have already applied various computational techniques to understand the effect of point defects in the thermal transport of ThO_2 . For instance, Cooper *et al.* [30] reported the degradation of thermal conductivity due to the nonuniform cation lattice of $(\text{U}_x\text{Th}_{1-x})\text{O}_2$ solid solutions, using the nonequilibrium molecular dynamics (NEMD) method, from 300 to 2000 K. Park *et al.* [31] used reverse nonequilibrium molecular dynamics (r-NEMD) to investigate the effect of vacancy and uranium substitutional defects in the thermal transport of ThO_2 . Rahman *et al.* [32] studied the dependence of thermal conductivity on fission-generated products (xenon and krypton) and vacancies in ThO_2 within 300–1500 K using NEMD simulations. Recently, Jin *et al.* [33], using NEMD simulations, reported the phonon-defect scattering cross section for a range of defects to be used with reduced-order analytical models. In all these studies, the quantum effects are ignored. The phonons follow the Boltzmann distribution instead of the physically correct Bose-Einstein distribution [34] and, therefore, are restricted to temperatures above the Debye temperature. But phonon-point defect scattering is more dominant at low temperatures; thus, molecular dynamics (MD)-based simulations are not ideal for describing phonon-point defect scattering. The other challenge for MD-based simulation is that the results depend on the accuracy of the interatomic potential. The work by Jin *et al.* [23] suggests that the empirical potential used previously needs to be further optimized for the robust prediction of thermal conductivity of ThO_2 , both in perfect crystals and in the presence of complex defects. Apart from MD simulations, Ryan *et al.* [5] studied the effect of point defects on the thermal conductivity of ThO_2 using the Klemens model for phonon relaxation times that result from the change in mass and induced lattice strain associated with point defects. This model computes the difference in force constants and atomic radii using MD simulation in ThO_2 . Again, this method is also limited to small

perturbations and does not consider the complete scattering to all orders.

Here, the phonon scattering due to point defects and their impact on the thermal conductivity of ThO₂ is described by an *ab initio* calculation utilizing the Green's function \mathbf{T} -matrix method. In the current study, we focus on the thermal conductivity degradation in ThO₂ due to a selected set of point defects, including the substitutions of transmutation and radioactive decay product helium (He_{Th}) and fission products, such as krypton (Kr_{Th}), zirconium (Zr_{Th}), iodine (I_{Th}), and xenon (Xe_{Th}) in thorium sites, along with other point defects, such as the single vacancy of thorium (V_{Th}) and oxygen (V_O) and three configurations of Schottky defects (SD₁₀₀, SD₁₁₀, SD₁₁₁).

II. METHODOLOGY

The lattice thermal conductivity (k_L) of ThO₂ with dilute point defect sites is calculated by summing over contributions from all phonons as

$$k_L = \frac{1}{3\Omega} \sum_{j\mathbf{q}} c_{j\mathbf{q}} v_{j\mathbf{q}}^2 \tau_{j\mathbf{q}}, \quad (1)$$

where Ω is the unit cell volume, $c_{j\mathbf{q}}$, $v_{j\mathbf{q}}$, and $\tau_{j\mathbf{q}}$ are the specific-heat capacity, group velocity, and relaxation time for the phonon in mode $j\mathbf{q}$, respectively, and j and \mathbf{q} represent the phonon branch index and wave vector, respectively. The inverse of the phonon relaxation time $\tau_{j\mathbf{q}}^{-1}$ is called the phonon scattering rate, and the total phonon scattering rate can be written as the sum of the contribution from different scattering mechanisms; in this work, we have considered contributions from three major scattering phenomena, including the intrinsic three-phonon scattering ($\tau_{j\mathbf{q},\text{anh}}^{-1}$) [35], phonon-isotope scattering ($\tau_{j\mathbf{q},\text{iso}}^{-1}$), and phonon-defect scattering ($\tau_{j\mathbf{q},\text{def}}^{-1}$) [14]:

$$\tau_{j\mathbf{q}}^{-1} = \tau_{j\mathbf{q},\text{anh}}^{-1} + \tau_{j\mathbf{q},\text{iso}}^{-1} + \tau_{j\mathbf{q},\text{def}}^{-1}. \quad (2)$$

For brevity, the equation governing the scattering rate for the intrinsic anharmonic scattering and the isotopic scattering rate is not provided here and can be found in Refs. [35,11], respectively. However, we provide a detailed discussion of the phonon-defect scattering. The phonon-defect scattering is computed using Green's function methodology using a \mathbf{T} matrix [14]. The advantages of using this approach is that, first, it captures the scattering due to variance in both mass and force constants, with the latter incorporating structural relaxation effects; second, it also accounts for complete scattering to all orders to capture the effect of resonances that would otherwise be missing in the lower-order perturbative methods. This approach is valid under the assumption of a random and dilute concentration of defects, which means the phonon scatters independently from different defects at a different location. The scattering cross section σ , an essential parameter in the phonon-defect scattering using the Green's function approach, is explained in detail in Ref. [15] and in the Supplemental Material of Ref. [18]. The scattering rate due to all possible elastic scattering processes of phonons by a random and dilute

distribution is given by Eq. (3),

$$\tau_{j\mathbf{q},\text{def}}^{-1} = \pi \chi_{\text{def}} \frac{\Omega}{V_{\text{def}}} \frac{1}{\omega_{j\mathbf{q}}} \sum_{j'\mathbf{q}'} |\langle j'\mathbf{q}' | \mathbf{T} | j\mathbf{q} \rangle|^2 \delta(\omega_{j'\mathbf{q}'}^2 - \omega_{j\mathbf{q}}^2), \quad (3)$$

where χ_{def} is the number fraction of defects, V_{def} is the volume of a defected supercell, $|j\mathbf{q}\rangle$ and $|j'\mathbf{q}'\rangle$ represent the incident and scattered phonon eigenstates, respectively, ω is the phonon angular frequency, and \mathbf{T} is the matrix associated with the point defect scatterer. The \mathbf{T} matrix is defined in terms of the perturbation matrix (\mathbf{V}) and the retarded Green's function [15] for the perfect structure (\mathbf{g}^+) as

$$\mathbf{T} = (\mathbf{I} - \mathbf{V}\mathbf{g}^+)^{-1}\mathbf{V}, \quad (4)$$

where (\mathbf{I}) is the identity matrix. Here, the perturbation matrix includes the mass (\mathbf{V}_M) and harmonic force constant (\mathbf{V}_K) differences between the perfect and defective systems, as shown below:

$$\mathbf{V} = (\mathbf{V}_M + \mathbf{V}_K). \quad (5)$$

The mass term is a diagonal matrix, with nonzero matrix elements corresponding to the defect site given as $\mathbf{V}_{M,i,i} = -(\frac{M'_i - M_i}{M_i})\omega^2$, where M'_i is the mass of the defect atom, M_i is the mass of the original atom at the i th site, and ω is the angular frequency of the incoming phonon [18]. Similarly, the presence of a point defect will also change the harmonic force constant around the defect, and this is included in the \mathbf{V}_K matrix, which is computed from the difference between the IFCs for the defective K' and perfect K structures as

$$\mathbf{V}_{K,i\alpha,k\beta} = \frac{K'_{i\alpha,k\beta} - K_{i\alpha,k\beta}}{\sqrt{M_i M_k}}. \quad (6)$$

Here, i and k are atom indices and α and β are the Cartesian axes. The Born approximation is achieved by Taylor series expansion of Eq. (4) and approximation $\mathbf{T} \approx \mathbf{V}$.

It is worth noting that \mathbf{V}_M is proportional to the square of the phonon frequency, and hence is smaller near the zero frequency, whereas \mathbf{V}_K is independent of the phonon frequency, and therefore a significant change in the harmonic force constants cannot be considered small at any frequency. Moreover, the IFCs are calculated at zero Kelvin, and hence the dependence of temperature on the scattering rate is not included. But as the phonon-defect scattering rates are frequency dependent, and the phonon population is both frequency and temperature dependent, the scattering rate indirectly influences the thermal conductivity as a function of temperature [13].

In this approach, the perturbation matrix is defined in real space and, to limit the size of the matrix, a cutoff radius r_{cut} needs to be enforced for the structural distortion. A large r_{cut} corresponding to the fifth-neighbor shell in ThO₂ is chosen for all the defects. Past this cutoff, the IFC changes are found to be negligible. Within r_{cut} , the changes in IFCs up to the second-nearest neighbors are considered. \mathbf{V}_K must obey the translational invariance rule and, when computed numerically, this symmetry must be enforced. This can be done by adding a minor correction to the harmonic IFCs of the perturbed system following a procedure outlined in [18].

We simplified the calculation represented by Eq. (3) with the use of the optical theorem. The total elastic scattering

of phonons by defects can be efficiently computed from the imaginary part of the diagonal element of the \mathbf{T} matrix, given by

$$\tau_{j\mathbf{q},\text{def}}^{-1} = -\chi_{\text{def}} \frac{\Omega}{V_{\text{def}}} \frac{1}{\omega_{j\mathbf{q}}} \text{Im}\{ \langle j\mathbf{q} | \mathbf{T} | j\mathbf{q} \rangle \}. \quad (7)$$

When using the optical theorem, the Born approximation requires inclusion of higher-order terms in the Taylor series expansion, $\mathbf{T} \approx \mathbf{V} + \mathbf{V}\mathbf{g}^+\mathbf{V}$.

III. SIMULATION DETAILS

All density functional theory [36] calculations in this work were performed using the projector-augmented wave (PAW) [37] method implemented in the plane-wave software package, Vienna Ab initio Simulation Package (VASP) [38], with the LDA [39] pseudopotential for the exchange and correlation. Also, it must be noted that no Hubbard U correction [40] was included in this work because it was previously shown that the Hubbard U correction offered no improvement to the property predictions of ThO_2 [41,42]. Moreover, ThO_2 is specifically used as a model material to UO_2 to avoid implementation of this correction. We performed the geometry optimization of ThO_2 (space group $Fm\bar{3}m$) on a primitive unit cell by minimizing the total energy with respect to changes in both cell parameters and atom positions using the conjugate gradient method. We obtained the energy convergence of ThO_2 , using an electron wave-vector grid and plane-wave energy cutoff of a $12 \times 12 \times 12$ mesh and 550 eV, respectively. The criteria for the electronic energy convergence was set at 10^{-8} eV. The lattice parameter for the obtained relaxed structure of ThO_2 at 0 K is 5.529 Å, which is consistent with the previously reported value [23] for the LDA functional from VASP and is comparable with the experimental lattice constant value of 5.60 Å [43]. However, it is worth noting that the GGA functional predicted the lattice constant better than the LDA; however, the thermal conductivity predicted by the GGA functional was found to be significantly lower. Hence the functional based on the LDA was used in this work. A $5 \times 5 \times 5$ supercell with 375 atoms and k points of $2 \times 2 \times 2$ were used to evaluate the harmonic force constants using the finite-displacement method as implemented in PHONOPY [44] and the calculated phonon dispersion spectra were compared with the experiment done by Bryan *et al.* [45], as shown in the Supplemental Material (SM), Fig. S5 [46]. The third-order force constants (anharmonic force constants) were also calculated using a $5 \times 5 \times 5$ supercell at the gamma point using THIRDORDER.PY [47], and the force cutoff distance was set to the fifth-nearest-neighbor atoms. In addition, because ThO_2 is a polar material, the nonanalytical contribution was considered, and the Born charges and dielectric constant required to evaluate the nonanalytical correction [48] were calculated using density functional perturbation theory [49]. The phonon-phonon scattering processes are evaluated using Fermi's golden rule from the cubic force constants. Finally, k_L was calculated using the iterative solutions of the Boltzmann transport equation (BTE) as implemented in ALMABTE [50]. All the k_L presented in this work are the fully iterative solutions of the Peierls-Boltzmann equation. The converged k_L values were obtained using a cubic force constant,

considering the fifth-nearest-neighbor interaction. The number of grid planes along each axis in the reciprocal space for solving the BTE was $24 \times 24 \times 24$.

All point defects considered in this work were created in a $5 \times 5 \times 5$ supercell. For vacancy defects, we removed a Th or O atom from their lattice position. We built the substitutional defects by replacing a Th atom with the corresponding fission products. The Schottky defects were formed by removing a unit of ThO_2 in the three-bound configuration of the SD, i.e., the SD_{100} , SD_{110} , and SD_{111} [51,52]. Each defected supercell was relaxed by keeping the cell volume constant. For the substitutional defects, a slight displacement of the defect atom or its nearest neighbors is introduced before relaxation to avoid the system getting trapped in a saddle point of the potential energy surface. We confirmed the dynamic stability of the relaxed structures by ensuring that the phonon band structure did not have any modes with imaginary frequency. The IFCs of the system with point defects were calculated using the finite-displacement method. The space-group symmetry of the supercell containing the point defect of V_{Th} and V_{O} was face centered cubic, while the space-group symmetry of the supercell containing the substitutional defects of He_{Th} , Kr_{Th} , Zr_{Th} , I_{Th} , and Xe_{Th} was orthorhombic, and the space-group symmetry of the supercell with the Schottky defects was orthorhombic for SD_{100} and SD_{110} and trigonal for SD_{111} . Space-group symmetries were determined using SPGLIB as implemented in the PHONOPY code. Finally, the phonon-defect scattering rates were calculated on a uniformly spaced $24 \times 24 \times 24$ q -point mesh with an $18 \times 18 \times 18$ grid for the Green's function, using the tetrahedron method to integrate over the Brillouin zone. Finally, to understand the charge transfer of the substituted defects to the neighboring atoms, the charge density difference plot was obtained using the VESTA software package [53] using the expression $\Delta\rho_{\text{diff}} = \rho[\text{ThO}_2 + \text{defect}] - \rho[\text{ThO}_2] - \rho[\text{defect}]$, where $\rho[\text{ThO}_2 + \text{defect}]$, $\rho[\text{ThO}_2]$, and $\rho[\text{defect}]$ are the charge density of ThO_2 with point defect, the pristine ThO_2 , and isolated atom corresponding to that particular defect, respectively.

IV. RESULTS AND DISCUSSION

We plotted the scattering rates (τ^{-1}) of each point defect type at a 1% concentration as a function of phonon frequency (ω) to provide insights into phonon scattering by various defects in ThO_2 . Figure 1 compares the τ^{-1} due to vacancy point defects to the anharmonic scattering rate of pristine ThO_2 at 300 K. The analysis of the phonon-defect scattering rate suggests that a thorium vacancy scatters the phonons more strongly than an oxygen vacancy. In vacancy defects, where the host atom is absent, the contribution to τ^{-1} comes from the IFC differences. To understand the extent of the force constant changes due to single vacancies of thorium or oxygen, we computed the Frobenius norm ratio of the IFC matrix. The values of the Frobenius norm ratio of the IFC matrix for the thorium vacancy (0.17) and oxygen vacancy (0.05) defects suggest that a thorium vacancy causes significantly more changes to the force constants than the oxygen vacancy, which explains why the thorium vacancy scatters the phonons more than the oxygen vacancy. Additionally, Fig. 1 also compares the frequency trends suggested by the Klemens model [6]

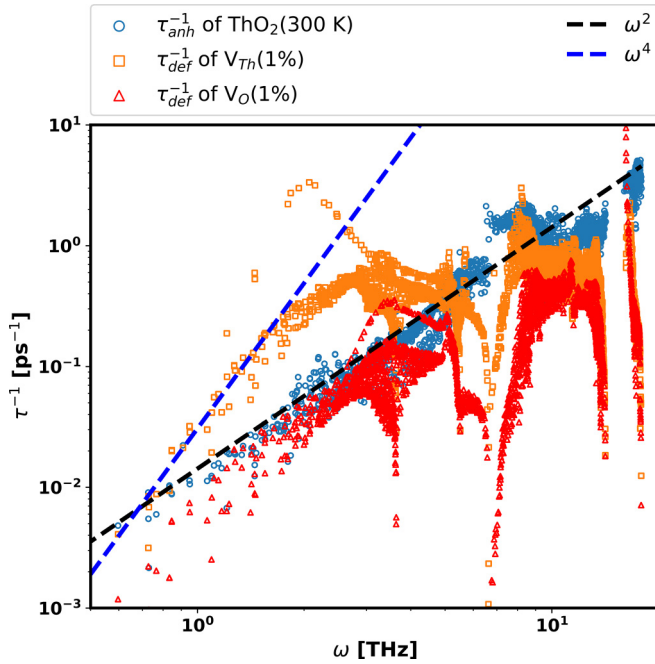


FIG. 1. Comparison of τ_{def}^{-1} of the V_{Th} (orange square) and V_{O} (red triangles) as a function of phonon frequency (ω) from the Green's function **T**-matrix method compared to τ^{-1} predicted by the Klemens model [anharmonic scattering (black dashed lines) and defect scattering (blue dashed lines)]. Hollow blue dots represent the anharmonic scattering (τ_{anh}^{-1}) of the pristine ThO_2 due to three-phonon interactions at 300 K.

for anharmonic scattering and point defects. According to the Klemens model, the anharmonic scattering rate follows an ω^2 dependence (black dashed lines) and the defect scattering has an ω^4 dependence (blue dashed lines). The latter is generally referred to as Rayleigh scattering. Klemens' model captures the anharmonic scattering in ThO_2 in agreement with the *ab initio* predictions. In contrast, Klemens' expression for point defect scattering, while correctly capturing the low-frequency trends, is unable to reproduce the high-frequency phonons, especially the optical modes which appear to have a much weaker dependence on frequency. One can argue that this is due to an oversimplified description of the phonon density of states employed in the Klemens expression not valid for high-frequency modes. Nevertheless, the Tamura model, which uses exact phonon dispersions, is also unable to capture high-frequency trends [11]. In fact the Tamura model makes the situation even worse. As the density of phonons increases at high frequency, it predicts scattering rates that are even larger than the one expected from Klemens' expressions [4,5]. The high-frequency overestimates of the Klemens and Tamura models is, in fact, due to their consideration of only the mass term, which has strong frequency dependence, whereas the perturbation due to IFC is frequency independent, suggesting that the IFC term dominates at high frequencies. Compared to the Green's function **T**-matrix methods, our calculations show that single-atom vacancy scattering centers are not well described by the Born approximation (Fig. 2), with a significant underestimation of τ^{-1} at low phonon frequencies and overestimation at high phonon frequencies for both thorium and

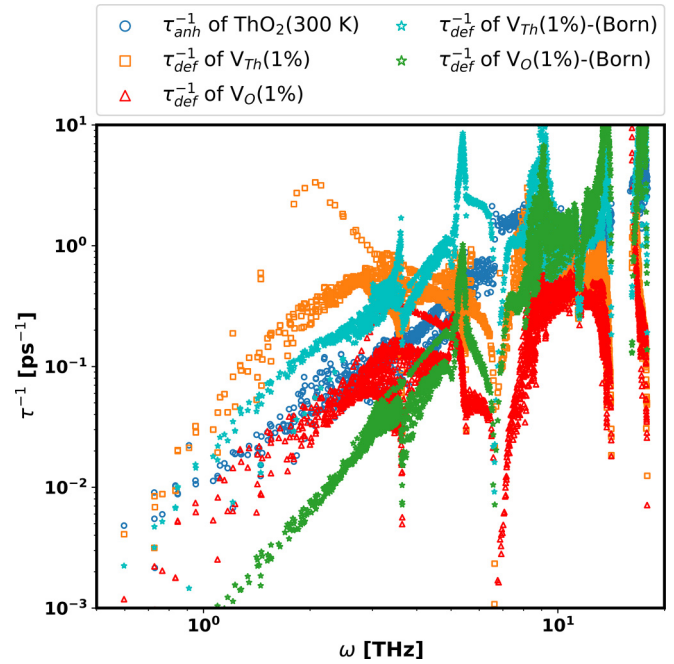


FIG. 2. Comparison of τ_{def}^{-1} of the V_{Th} (orange square) and V_{O} (red triangles) as a function of phonon frequency (ω) from the Green's function **T**-matrix method compared to the Born approximation for V_{Th} (cyan star) and V_{O} (green star). Hollow blue dots represent the anharmonic scattering (τ_{anh}^{-1}) of pristine ThO_2 due to three-phonon interactions at 300 K.

oxygen vacancies. It is worth noting that there are prominent peaks observed at 2 THz for thorium vacancies and 3 THz for oxygen vacancies. Further modal analysis reveals that these peaks are associated with longitudinal acoustic (LA) waves and appear at the location where the transverse acoustic (TA) mode has a large density of states. Under the Born approximation, the scattering of LA modes to TA is not possible as the momentum is not conserved. Previously, such behavior in silicon carbide and gallium arsenide has been attributed to resonant scattering [18,54]. The Green's function approach considers full scattering to all orders, thus capturing the effect that leads to enhanced phonon scattering due to the emergence of localized modes. Apart from vacancy defects, neutron irradiation will introduce substitutional defects. To discern the phonon scattering due to the substitutional atoms in ThO_2 , we considered some common fission products such as Kr, Zr, I, and Xe as well as He in the thorium sites. Our reason for only considering thorium sites and not oxygen sites is that the Th atom's vibration governs the acoustic modes and contributes $\approx 70\%$ of the thermal conductivity [22]. Hence, defects on the Th sites, particularly those that have a large mass or IFC variance, can degrade the thermal conductivity more significantly than those of the light O atoms. Unlike vacancy defects, the scattering from substitutional atoms arises from the mass difference between the substitutional and host atom and the IFCs variations around the substituted site due to the structural relaxation and modified chemical environment.

The previous study using the same methodology has shown that in general, substitutional atoms scatter phonons less effectively than vacancies [13]. Our ThO_2 results as shown in

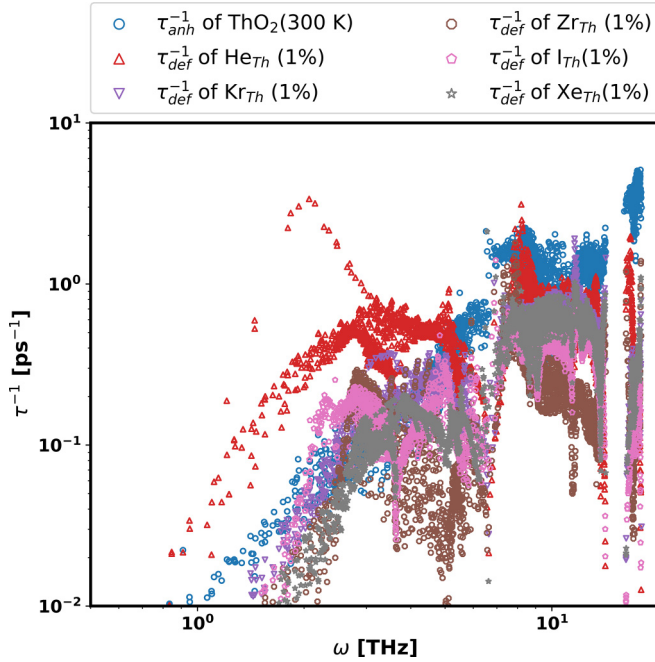


FIG. 3. Scattering rates (τ_{def}^{-1}) of phonons as a function of phonon frequency (ω) due to substitutional point defects of He_{Th} (up-pointing crimson red triangle), Kr_{Th} (down-pointing purple triangle), Zr_{Th} (brown octagon), I_{Th} (pink pentagon), and Xe_{Th} (gray star) in thorium sites compared to τ_{anh}^{-1} of the pristine ThO_2 due to three-phonon interactions at 300 K (blue dots).

Fig. 3 indicate that a substitution by a significantly lighter He atom results in phonon scattering with a strength comparable to thorium vacancy, to the extent that they overlap. The primary reason for He substitution to strongly scatter phonons is because He as a light chemically inert atom induces a force constant variance very similar to that of the thorium vacancy (see Table 1 in the SM [46]). As expected, a similar resonant peak as seen in athorium vacancy is also observed for a helium substitution at the same frequency.

Among the other substitutional atoms, intuitively based on mass differences, one expects the scattering strength to be $\text{He}_{\text{Th}} > \text{Kr}_{\text{Th}} > \text{Zr}_{\text{Th}} > \text{I}_{\text{Th}} > \text{Xe}_{\text{Th}}$. However, contrary to this intuition, the predicted scattering strengths of the fission products were $\text{He}_{\text{Th}} > \text{Kr}_{\text{Th}} > \text{I}_{\text{Th}} > \text{Xe}_{\text{Th}} > \text{Zr}_{\text{Th}}$, where the Zr_{Th} substitution scattered phonons the least. To understand why the Zr_{Th} substitution showed minimal phonon scattering, we computed the Frobenius norm ratio of the IFC matrix (see Table 1 in the SM [46]) and found that the force constant perturbations were the lowest when Zr was in thorium sites. This can be attributed to the fact that unlike noble gas elements (He, Xe, and Kr) and electronegative elements (I), Zr is an electropositive element, and Zr in a cation lattice site can donate electrons to the oxygen and form bonds. The charge transfer in the substitutional defects was quantified (see Fig. S3 in the SM [46]) to provide insights into the redistribution of charge and bond strength. In the case of a Zr substitution, the charge transfer takes place from the Zr atom out towards the surrounding O atoms. Also, the charge accumulated around the Zr atom is negligible since Th and Zr have similar ionic charges. This observation clearly indicates

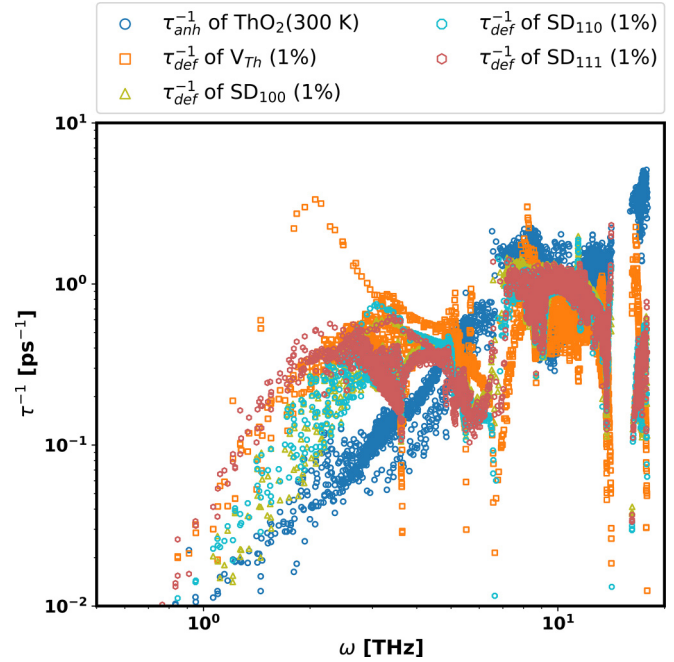


FIG. 4. Scattering rates (τ_{def}^{-1}) of phonons by three different configurations of the Schottky defects [SD_{100} (up-pointing green triangle), SD_{110} (blue octagon), SD_{111} (red pentagon)] in ThO_2 compared to the τ_{def}^{-1} of the V_{Th} and the τ_{anh}^{-1} of the pristine ThO_2 due to three-phonon interactions at 300 K.

that local chemical modification can significantly impact force constant perturbations and, thus, phonon scattering.

Finally, as an example of larger defects, we investigated the role of Schottky defects in ThO_2 in scattering the phonons, as depicted in Fig. 4. Among the three different Schottky defect configurations, the scattering strengths are $\text{SD}_{111} > \text{SD}_{110} > \text{SD}_{100}$, which indicates that ThO_2 with an SD_{111} defect scatters phonons the most.

Using the calculated scattering rates, including the anharmonic, isotropic, and phonon-defect scattering, the k_L of ThO_2 was computed using an iterative solution of the BTE. Figure 5 shows the k_L of pristine ThO_2 and ThO_2 with vacancy defects as a function of temperature. Thorium vacancies caused the most significant reduction in thermal conductivity, consistent with the observation made with the phonon-point defect scattering rate (Fig. 1). Oxygen vacancies at 0.001 concentration caused a marginal decrease in thermal conductivity. The theoretical results are compared with the recent experimental measurement done on a proton-irradiated single crystal of ThO_2 at a small dose of 0.004 displacements per atom [55]. At these low-dose and room-temperature irradiation conditions, thorium vacancies and interstitials are the most likely defects, as predicted by the rate theory calculation presented in Dennett *et al.* [3]. However, current T-matrix formalism cannot be applied to interstitial defects located at octahedral sites [56]; therefore, to account for this type of defects, some assumptions need to be made. The scattering cross sections of the vacancies and interstitials are similar based on the NEMD simulations by Jin *et al.* [33]. Based on these arguments, we estimate that 0.004 dpa corresponds to an equivalent concentration of V_{Th} to be $\approx 0.25\%$. Using

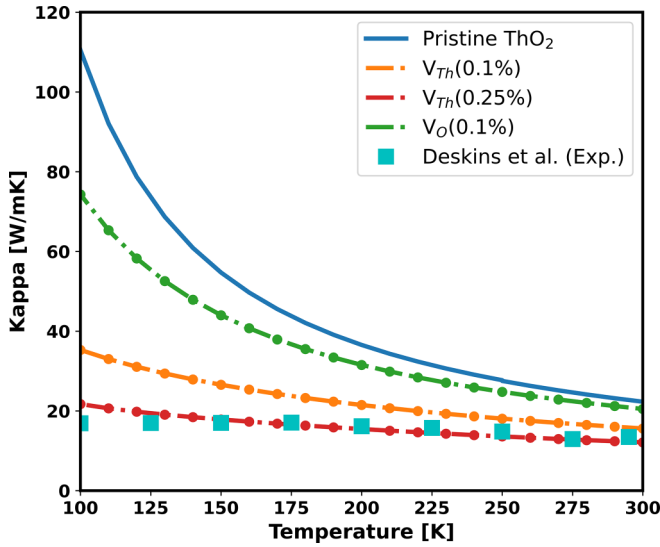


FIG. 5. The calculated k_L of ThO_2 with vacancy defects [V_{Th} (0.1% and 0.25%) and V_{O} (0.1%)] at a lower-temperature range of 100–300 K. The experiments are from Deskins *et al.* [55], corresponding to ThO_2 single crystals irradiated with 2 MeV protons to a dose of 0.004 displacements per atom at room temperature.

the concentration of 0.25% V_{Th} yields an excellent agreement between the predicted and the experimental thermal conductivity. Figure 6 shows the degradation of thermal conductivity due to substitutional defects. Among the considered elements, He with the largest perturbation caused the largest reduction in thermal conductivity, followed by $\text{Kr}_{\text{Th}} > \text{I}_{\text{Th}} > \text{Xe}_{\text{Th}} > \text{Zr}_{\text{Th}}$. Figure 7 shows k_L as a function of defect concentration at 300 K. The results indicate that for point defects to impact thermal transport, the concentration has to be of the order of 10^{-2} atomic %. For brevity, the k_L degradation for 1% defect concentrations for all the vacancies and substitutional

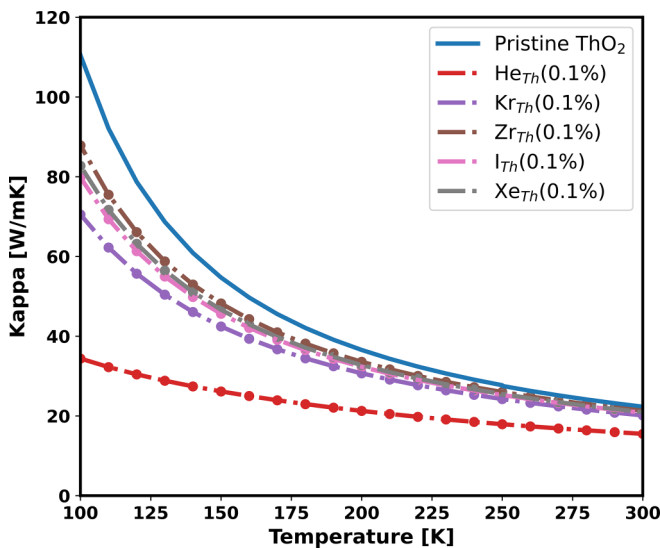


FIG. 6. The calculated k_L of ThO_2 with 0.1% fission products of He_{Th} , Kr_{Th} , Zr_{Th} , I_{Th} , and Xe_{Th} at a lower-temperature range of 100–300 K.

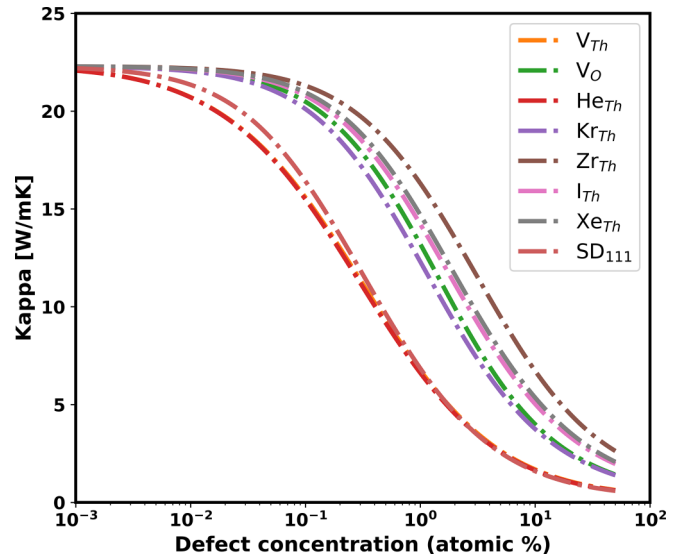


FIG. 7. ThO_2 k_L variation with defect concentration for V_{Th} , V_{O} , He_{Th} , Kr_{Th} , Zr_{Th} , I_{Th} , Xe_{Th} , and SD_{111} at 300 K.

defects, the k_L reduction due to the Schottky defects for two different concentrations of 0.1% and 1%, and the thermal conductivity degradation at high temperatures are provided in the SM (Figs. S1 and S2) [46]. The results for Schottky defects suggest that among the three different configurations, the SD_{111} impacted thermal transport the most, followed by SD_{110} and SD_{100} . All these observations shed light on the effect of point defects on thermal transport in thorium dioxide and help in understanding the behavior of nuclear reactors [2]. Lastly, we should point out that experimental measurements of thermal conductivity in irradiated ThO_2 and $(\text{Th},\text{U})\text{O}_2$ alloys provided evidence of the presence of phonon resonant scattering as the temperature dependence deviated from a $1/T$ trend at low temperatures [55,57]. Our phonon scattering rates, shown in Figs. 1 and 3, provide some indication of the resonances, which for other materials have resulted in the calculated thermal conductivity departing from a $1/T$ trend [54]. However, our calculated thermal conductivity values reported in Figs. 5 and 6 do not reflect this. This observation suggests that further work is needed to improve estimation of low-temperature thermal conductivity.

V. CONCLUSION

Using a fully *ab initio* Green's function **T**-matrix method, we have presented an extensive analysis of the phonon-defect scattering rate of ThO_2 with point defects. The phonon-point defect scattering rates were unified with the Peierls-Boltzmann transport equation to determine the effects of defects on phonon thermal conductivity in ThO_2 . The results revealed that among all the intrinsic defects considered in this work, the thorium vacancy and helium substitution in the thorium site caused the most significant reduction in the thermal conductivity of ThO_2 . The similar behaviors of the thorium vacancy and helium substitution were due to the comparable force constant difference induced by these two defects. Also, a large peak, which is a signature of resonant

scattering, was observed in the case of a thorium vacancy and helium substitution. Among the substitutional defects, the zirconium substitution had the smallest reduction in thermal conductivity, despite having a significant mass difference compared to iodine and xenon. The primary reason for the relatively weaker scattering by zirconium substitution is its similar valency to thorium, thus enabling bond formation with oxygen, inducing the least force constant differences. Unlike zirconium, the chemical environment due to helium, krypton, iodine, and xenon creates a larger force constant difference, leading to higher scattering rates. This study revealed that the modification of the local chemical environment and the associated structure and force variations caused by substitutional defects should be considered while studying phonon-defect scattering. This work enhances our understanding of the phonon-defect scattering due to various fission products in ThO₂, which will serve as a benchmark for analytical models and help improve the engineering-scale modeling predictions for nuclear reactor design.

ACKNOWLEDGMENTS

This work was supported by the Center for Thermal Energy Transport under Irradiation (TETI), an Energy Frontier Research Center (EFRC) funded by the U.S. Department of Energy, Office of Science, and Office of Basic Energy Sciences. The authors also acknowledge that this research made use of the resources of the High Performance Computing Center at Idaho National Laboratory, which is supported by the Office of Nuclear Energy of the U.S. Department of Energy and the Nuclear Science User Facilities under Contract No. DE-AC07-05ID14517. The authors of this manuscript has been supported by the Battelle Energy Alliance, LLC under Contract No. DE-AC07-05ID14517 with the U.S. Department of Energy. The United States Government retains and the publisher, by accepting the article for publication, acknowledges that the U.S. Government retains a nonexclusive, paid-up, irrevocable, worldwide license to publish or reproduce the published form of this manuscript, or allow others to do so, for U.S. Government purposes.

-
- [1] V. Dekoussar, G. R. Dyck, A. Galperin, C. Ganguly, M. Todosow, and M. Yamawaki, *Thorium Fuel Cycle - Potential Benefits and Challenges*, TECDOC Series No. 1450 (International Atomic Energy Agency, Vienna, 2005).
- [2] D. H. Hurley, A. El-Azab, M. S. Bryan, M. W. D. Cooper, C. A. Dennett, K. Gofryk, L. He, M. Khafizov, G. H. Lander, M. E. Manley, J. M. Mann, C. A. Marianetti, K. Rickert, F. A. Selim, M. R. Tonks, and J. P. Wharry, Thermal energy transport in oxide nuclear fuel, *Chem. Rev.* **122**, 3711 (2022).
- [3] C. A. Dennett, W. R. Deskins, M. Khafizov, Z. Hua, A. Khanolkar, K. Bawane, L. Fu, J. M. Mann, C. A. Marianetti, L. He, D. H. Hurley, and A. El-Azab, An integrated experimental and computational investigation of defect and microstructural effects on thermal transport in thorium dioxide, *Acta Mater.* **213**, 116934 (2021).
- [4] R. Gurunathan, R. Hanus, M. Dylla, A. Katre, and G. J. Snyder, Analytical models of phonon-point-defect scattering, *Phys. Rev. Appl.* **13**, 034011 (2020).
- [5] W. R. Deskins, A. Hamed, T. Kumagai, C. A. Dennett, J. Peng, M. Khafizov, D. Hurley, and A. El-Azab, Thermal conductivity of ThO₂: Effect of point defect disorder, *J. Appl. Phys.* **129**, 075102 (2021).
- [6] P. G. Klemens, The scattering of low-frequency lattice waves by static imperfections, *Proc. Phys. Soc. London, Sect. A* **68**, 1113 (1955).
- [7] M. Asheghi, K. Kurabayashi, R. Kasnavi, and K. E. Goodson, Thermal conduction in doped single-crystal silicon films, *J. Appl. Phys.* **91**, 5079 (2002).
- [8] J. Zou, D. Kotchetkov, A. A. Balandin, D. I. Florescu, and F. H. Pollak, Thermal conductivity of GaN films: Effects of impurities and dislocations, *J. Appl. Phys.* **92**, 2534 (2002).
- [9] R. Fletcher, Scattering of phonons by dislocations in potassium, *Phys. Rev. B* **36**, 3042 (1987).
- [10] H. Malekpour, P. Ramnani, S. Srinivasan, G. Balasubramanian, D. L. Nika, A. Mulchandani, R. K. Lake, and A. A. Balandin, Thermal conductivity of graphene with defects induced by electron beam irradiation, *Nanoscale* **8**, 14608 (2016).
- [11] S. I. Tamura, Isotope scattering of dispersive phonons in Ge, *Phys. Rev. B* **27**, 858 (1983).
- [12] J. J. Sakurai, *Advanced Quantum Mechanics*, Always Learning (Pearson Education, Incorporated, Lebanon, Indiana, USA, 1967).
- [13] C. A. Polanco and L. Lindsay, Thermal conductivity of InN with point defects from first principles, *Phys. Rev. B* **98**, 014306 (2018).
- [14] N. Mingo, K. Esfarjani, D. A. Broido, and D. A. Stewart, Cluster scattering effects on phonon conduction in graphene, *Phys. Rev. B* **81**, 045408 (2010).
- [15] A. Kundu, N. Mingo, D. A. Broido, and D. A. Stewart, Role of light and heavy embedded nanoparticles on the thermal conductivity of SiGe alloys, *Phys. Rev. B* **84**, 125426 (2011).
- [16] N. A. Katcho, J. Carrete, W. Li, and N. Mingo, Effect of nitrogen and vacancy defects on the thermal conductivity of diamond: An *ab initio* Green's function approach, *Phys. Rev. B* **90**, 094117 (2014).
- [17] N. H. Protik, J. Carrete, N. A. Katcho, N. Mingo, and D. Broido, *Ab initio* study of the effect of vacancies on the thermal conductivity of boron arsenide, *Phys. Rev. B* **94**, 045207 (2016).
- [18] A. Katre, J. Carrete, B. Dongre, G. K. H. Madsen, and N. Mingo, Exceptionally strong phonon scattering by B substitution in cubic SiC, *Phys. Rev. Lett.* **119**, 075902 (2017).
- [19] A. Katre, J. Carrete, T. Wang, G. K. H. Madsen, and N. Mingo, Phonon transport unveils the prevalent point defects in GaN, *Phys. Rev. Mater.* **2**, 050602(R) (2018).
- [20] C. A. Polanco and L. Lindsay, *Ab initio* phonon point defect scattering and thermal transport in graphene, *Phys. Rev. B* **97**, 014303 (2018).
- [21] J. Liu, Z. Dai, X. Yang, Y. Zhao, and S. Meng, Lattice thermodynamic behavior in nuclear fuel ThO₂ from first principles, *J. Nucl. Mater.* **511**, 11 (2018).

- [22] L. Malakkal, A. Prasad, E. Jossou, J. Ranasinghe, B. Szpunar, L. Bichler, and J. Szpunar, Thermal conductivity of bulk and porous ThO₂: Atomistic and experimental study, *J. Alloys Compd.* **798**, 507 (2019).
- [23] M. Jin, M. Khafizov, C. Jiang, S. Zhou, C. A. Marianetti, M. S. Bryan, M. E. Manley, and D. H. Hurley, Assessment of empirical interatomic potential to predict thermal conductivity in ThO₂ and UO₂, *J. Phys.: Condens. Matter* **33**, 275402 (2021).
- [24] E. Xiao, H. Ma, M. S. Bryan, L. Fu, J. M. Mann, B. Winn, D. L. Abernathy, R. P. Hermann, A. R. Khanolkar, C. A. Dennett, D. H. Hurley, M. E. Manley, and C. A. Marianetti, Validating first-principles phonon lifetimes via inelastic neutron scattering, *Phys. Rev. B* **106**, 144310 (2022).
- [25] M. Mann, D. Thompson, K. Serivalsatit, T. M. Tritt, J. Ballato, and J. Kolis, Hydrothermal growth and thermal property characterization of ThO₂ single crystals, *Cryst. Growth Des.* **10**, 2146 (2010).
- [26] J. Sun, A. Ruzsinszky, and J. P. Perdew, Strongly constrained and appropriately normed semilocal density functional, *Phys. Rev. Lett.* **115**, 036402 (2015).
- [27] J. Ferrigno, S. Adnan, and M. Khafizov, Influence of point defect accumulation on in-pile thermal conductivity degradation: Fuel rod defect distribution and deviation between in-pile and post-irradiation thermal conductivity, *J. Nucl. Mater.* **573**, 154108 (2023).
- [28] M. Khafizov, V. Chauhan, Y. Wang, F. Riyad, N. Hang, and D. H. Hurley, Investigation of thermal transport in composites and ion beam irradiated materials for nuclear energy applications, *J. Mater. Res.* **32**, 204 (2017).
- [29] C. A. Dennett, Z. Hua, A. Khanolkar, T. Yao, P. K. Morgan, T. A. Prusnick, N. Poudel, A. French, K. Gofryk, L. He, L. Shao, M. Khafizov, D. B. Turner, J. M. Mann, and D. H. Hurley, The influence of lattice defects, recombination, and clustering on thermal transport in single crystal thorium dioxide, *APL Mater.* **8**, 111103 (2020).
- [30] M. Cooper, S. Middleburgh, and R. Grimes, Modelling the thermal conductivity of U_xTh_{1-x}O₂ and U_xPu_{1-x}O₂, *J. Nucl. Mater.* **466**, 29 (2015).
- [31] J. Park, E. B. Farfán, K. Mitchell, A. Resnick, C. Enriquez, and T. Yee, Sensitivity of thermal transport in thorium dioxide to defects, *J. Nucl. Mater.* **504**, 198 (2018).
- [32] M. Rahman, B. Szpunar, and J. Szpunar, Dependence of thermal conductivity on fission-product defects and vacancy concentration in thorium dioxide, *J. Nucl. Mater.* **532**, 152050 (2020).
- [33] M. Jin, C. A. Dennett, D. H. Hurley, and M. Khafizov, Impact of small defects and dislocation loops on phonon scattering and thermal transport in ThO₂, *J. Nucl. Mater.* **566**, 153758 (2022).
- [34] Y. Zhou, Z. Fan, G. Qin, J.-Y. Yang, T. Ouyang, and M. Hu, Methodology perspective of computing thermal transport in low-dimensional materials and nanostructures: The old and the new, *ACS Omega* **3**, 3278 (2018).
- [35] J. M. Ziman, *Electrons and Phonons: The Theory of Transport Phenomena in Solids* (Oxford University Press, University of Bristol, 2001).
- [36] W. Kohn and L. J. Sham, Self-consistent equations including exchange and correlation effects, *Phys. Rev.* **140**, A1133 (1965).
- [37] P. E. Blöchl, Projector augmented-wave method, *Phys. Rev. B* **50**, 17953 (1994).
- [38] G. Kresse and J. Furthmüller, Efficient iterative schemes for *ab initio* total-energy calculations using a plane-wave basis set, *Phys. Rev. B* **54**, 11169 (1996).
- [39] J. P. Perdew and A. Zunger, Self-interaction correction to density-functional approximations for many-electron systems, *Phys. Rev. B* **23**, 5048 (1981).
- [40] S. L. Dudarev, G. A. Botton, S. Y. Savrasov, C. J. Humphreys, and A. P. Sutton, Electron-energy-loss spectra and the structural stability of nickel oxide: An LSDA+U study, *Phys. Rev. B* **57**, 1505 (1998).
- [41] A. E. Shields, D. Santos-Carballal, and N. H. de Leeuw, A density functional theory study of uranium-doped thoria and uranium adatoms on the major surfaces of thorium dioxide, *J. Nucl. Mater.* **473**, 99 (2016).
- [42] Y. Lu, Y. Yang, and P. Zhang, Thermodynamic properties and structural stability of thorium dioxide, *J. Phys.: Condens. Matter* **24**, 225801 (2012).
- [43] M. Idiri, T. Le Bihan, S. Heathman, and J. Rebizant, Behavior of actinide dioxides under pressure: UO₂ and ThO₂, *Phys. Rev. B* **70**, 014113 (2004).
- [44] A. Togo and I. Tanaka, First principles phonon calculations in materials science, *Scr. Mater.* **108**, 1 (2015).
- [45] B. Matthew, F. Lyuwen, K. Rickert, T. David, T. A. Prusnick, M. Matthew, A. Douglas, M. Chris, and M. Michael, Nonlinear propagating modes beyond the phonons in fluorite-structured crystals, *Commun. Phys.* **3**, 217 (2020).
- [46] See Supplemental Material at <http://link.aps.org/supplemental/10.1103/PhysRevMaterials.8.025401> for the thermal conductivity degradation at 1% concentration of point defects as a function of temperature, comparison of the charge density plot of various substitutional defects, comparison of the scattering rate due to mass and force constant perturbation separately, the phonon dispersion spectra of ThO₂, the frobenius norm of force constant changes for various defects considered, phonon defect scattering plots for individual defects, and the relaxed structure and the neighboring atom distance.
- [47] W. Li, J. Carrete, N. A. Katcho, and N. Mingo, ShengBTE: A solver of the Boltzmann transport equation for phonons, *Comput. Phys. Commun.* **185**, 1747 (2014).
- [48] W. Yi, S. Shun-Li, F. Huazhi, L. Zi-Kui, and C. L. Qing, First-principles calculations of lattice dynamics and thermal properties of polar solids, *npj Comput. Mater.* **2**, 16006 (2016).
- [49] S. Baroni, S. De Gironcoli, A. Dal Corso, and P. Giannozzi, Phonons and related crystal properties from density-functional perturbation theory, *Rev. Mod. Phys.* **73**, 515 (2001).
- [50] J. Carrete, B. Vermeersch, A. Katre, A. van Roekeghem, T. Wang, G. K. Madsen, and N. Mingo, almaBTE: A solver of the space-time dependent Boltzmann transport equation for phonons in structured materials, *Comput. Phys. Commun.* **220**, 351 (2017).
- [51] M. Iwasawa, T. Ohnuma, Y. Chen, Y. Kaneta, H. Geng, A. Iwase, and M. Kinoshita, First-principles study on cerium ion behavior in irradiated cerium dioxide, *J. Nucl. Mater.* **393**, 321 (2009).
- [52] B. Dorado, M. Freyss, and G. Martin, GGA+U study of the incorporation of iodine in uranium dioxide, *Eur. Phys. J. B* **69**, 203 (2009).
- [53] K. Momma and F. Izumi, VESTA: A three-dimensional visualization system for electronic and structural analysis, *J. Appl. Crystallogr.* **41**, 653 (2008).

- [54] A. Kundu, F. Otte, J. Carrete, P. Erhart, W. Li, N. Mingo, and G. K. H. Madsen, Effect of local chemistry and structure on thermal transport in doped GaAs, *Phys. Rev. Mater.* **3**, 094602 (2019).
- [55] W. R. Deskins, A. Khanolkar, S. Mazumder, C. A. Dennett, K. Bawane, Z. Hua, J. Ferrigno, L. He, J. M. Mann, M. Khafizov, D. H. Hurley, and A. El-Azab, A combined theoretical-experimental investigation of thermal transport in low-dose irradiated thorium dioxide, *Acta Mater.* **241**, 118379 (2022).
- [56] C. Jiang, L. He, C. A. Dennett, M. Khafizov, J. M. Mann, and D. H. Hurley, Unraveling small-scale defects in irradiated ThO₂ using kinetic Monte Carlo simulations, *Scr. Mater.* **214**, 114684 (2022).
- [57] Z. Hua, S. Adnan, A. R. Khanolkar, K. Rickert, D. B. Turner, T. A. Prusnick, J. M. Mann, D. H. Hurley, M. Khafizov, and C. A. Dennett, Thermal conductivity suppression in uranium-doped thorium dioxide due to phonon-spin interactions, *J. Materiomics* (2023).